

# Lattice Dynamics and Vibrational Spectra of Lithium Manganese Oxides: A Computer Simulation and Spectroscopic Study

Brett Ammundsen,<sup>†,‡,§</sup> Gary R. Burns,<sup>\*,‡</sup> M. Saiful Islam,<sup>||</sup> Hirofumi Kanoh,<sup>⊥</sup> and Jacques Rozière<sup>†</sup>

Laboratoire des Agrégats Moléculaires et Matériaux Inorganiques (LAMMI), ESA 5072 CNRS, Université Montpellier 2, Place Eugène Bataillon, 34095 Montpellier Cédex 5, France, School of Chemical and Physical Sciences, Victoria University of Wellington, P.O. Box 600, Wellington, New Zealand, Department of Chemistry, University of Surrey, Guildford, Surrey GU2 5XH, U. K., and Shikoku National Industrial Research Institute, 2217-14 Hayashi-cho, Takamatsu, 761-03, Japan

Received: November 11, 1998; In Final Form: April 13, 1999

The lattice vibrational modes of spinel-structured lithium manganese oxides have been calculated using atomistic modeling methods. The simulations allow the Raman and infrared spectra of lithiated, fully delithiated, and partially delithiated phases to be assigned for the first time. Calculations for the spinels  $\text{LiMn}_2\text{O}_4$ ,  $\lambda\text{-MnO}_2$ , and  $\text{Li}_{0.5}\text{Mn}_2\text{O}_4$  are compared with experimental Raman data measured for thin films of the oxides coated on a platinum electrode. The appearance of a number of new bands in the Raman spectrum of  $\text{LiMn}_2\text{O}_4$  following partial extraction of lithium is shown to result from local lowering of the symmetry and Raman activation of modes which are optically inactive or only infrared active in  $\text{LiMn}_2\text{O}_4$ . The results support a model for the  $\text{Li}_{0.5}\text{Mn}_2\text{O}_4$  lattice in which the lithium ions are ordered. The deformation vibrations of lattice hydroxyl “defects” in  $\lambda\text{-MnO}_2$  have also been calculated; comparison of the calculated and experimental vibrational data supports a model in which hydroxyl species are localized at octahedral Mn vacancies.

## 1. Introduction

Spinel phases of lithium manganese oxide are important positive electrode and lithium-selective ion-sorption materials. In these applications, the octahedral manganese–oxygen sublattice serves as a host framework within which lithium ions are withdrawn and inserted. The advantages of using vibrational spectroscopy to examine structural changes in these compounds have recently been described by Richardson et al.<sup>1</sup> Vibrational spectroscopy is sensitive to the short-range environment of oxygen coordination around both manganese and lithium ions. When a number of different environments are present in the same material, the vibrational spectrum is a superposition of the spectra of all local structures, in contrast to diffraction data which gives a weighted average of similar interplanar spacings. The bands in infrared and Raman spectroscopy are sensitive to coordination geometry and oxidation states and are, relative to powder X-ray diffraction, unaffected by crystallite size or the degree of long-range order. This is particularly advantageous for electrode materials where the crystallinity and homogeneity of the compound is frequently degraded by repeated lithium extraction–insertion cycles.

Given the large quantity of useful structural information contained in the vibrational spectra of lithium manganese oxides, there is a need for a fundamental description of the lattice vibrations, particularly those that are infrared and Raman active.

However, to our knowledge, lattice dynamical calculations have never been reported for a spinel lithium manganese oxide. Infrared spectra have been published in a number of studies,<sup>2–9</sup> but the interpretations have been mainly limited to empirical comparisons and there is considerable uncertainty in the assignments of the bands observed. There are no detailed analyses of the Raman spectra of lithium manganese oxides, presumably because in the absence of any resonance enhancement they are relatively weak Raman scatterers and without single-crystal data it is difficult to assign the observed bands.

To resolve these problems, we have used atomistic simulation methods based on an interatomic potential model to determine the normal modes of the zone-center ( $k = 0$ ) lattice phonons in spinel  $\text{LiMn}_2\text{O}_4$  and the lithium-extracted phases  $\text{Li}_{0.5}\text{Mn}_2\text{O}_4$  and  $\lambda\text{-MnO}_2$ . We compare the results of these calculations with Raman data recorded for both bulk phases and thin-film lithium manganese oxides coated on a platinum electrode and infrared data recorded for bulk phases. Finally, we apply our potential model to a vibrational analysis of the lattice dynamics of protons inserted in spinel  $\text{MnO}_2$ .

## 2. Methods

**2.1. Atomistic Simulation.** The simulation techniques have been described comprehensively elsewhere<sup>10–13</sup> and have been previously applied to a range of mixed metal oxides.<sup>14–18</sup> The calculations were carried out using energy minimization procedures embodied in the GULP code. The interatomic potentials are based on the Born model of the solid, which includes a long-range Coulombic interaction and a short-range term to model overlap repulsions and van der Waals forces,

$$V_{ij}(r_{ij}) = [-Z_i Z_j e^2 / r] + [A_{ij} \exp(-r/\rho_{ij}) - C/r_{ij}^6] \quad (1)$$

\* To whom correspondence should be addressed. Telephone: +64 4 463 5947. Fax: +64 4 495 5241. E-mail: gary.burns@vuw.ac.nz.

<sup>†</sup> Université Montpellier 2.

<sup>‡</sup> Victoria University of Wellington.

<sup>§</sup> Present address: Pacific Lithium Limited, PO Box 90725, Auckland, New Zealand.

<sup>||</sup> University of Surrey.

<sup>⊥</sup> Shikoku National Industrial Research Institute.

**TABLE 1: Interatomic Potentials for the Lithium Manganates**

(i) Short-Range			
interaction <sup>a</sup>	A (eV)	$\rho$ (Å)	C (eV Å <sup>6</sup> )
Mn <sup>4+</sup> ...O <sup>2-</sup>	1345.15	0.324	0.0
Mn <sup>3+</sup> ...O <sup>2-</sup>	1267.5	0.324	0.0
Li <sup>+</sup> ...O <sup>2-</sup>	426.48	0.3000	0.0
O <sup>2-</sup> ...O <sup>2-</sup>	22764.3	0.1490	43.0
(ii) Shell Model			
species	Y (e)	k (eV Å <sup>-2</sup> )	
Mn <sup>4+</sup>	4.00	150	
Mn <sup>3+</sup>	3.00	850	
O <sup>2-</sup>	-2.96	57	

<sup>a</sup> Potential cutoff = 12 Å.**TABLE 2: Calculated and Experimental Crystal Properties for LiMn<sub>2</sub>O<sub>4</sub> and  $\lambda$ -MnO<sub>2</sub>**

(a) Unit Cell Parameters			
		$a_0$ (calcd) (Å)	$a_0$ (exptl) (Å)
LiMn <sub>2</sub> O <sub>4</sub>		8.2478	8.2470
$\lambda$ -MnO <sub>2</sub>		8.0515	8.0445
(b) Atomic Coordinates (Fd3m)			
species		$x,y,z$ (calcd)	$x,y,z$ (exptl)
LiMn <sub>2</sub> O <sub>4</sub>	Mn <sup>3+</sup> , Mn <sup>4+</sup> (16d)	0.5	0.5
	Li <sup>+</sup> (8a)	0.125	0.125
	O <sup>2-</sup> (32e)	0.2630	0.2625
$\lambda$ -MnO <sub>2</sub>	Mn <sup>4+</sup> (16d)	0.5	0.5
	O <sup>2-</sup> (32e)	0.2632	0.2631

The electronic polarizability of the ions is described by the shell model, which is effective in simulating the dielectric and lattice dynamical properties of metal oxides. It should be stressed that employing such a potential model does not necessarily mean that the electron distribution corresponds to a fully ionic system and that the validity of the potential model is assessed primarily by its ability to reproduce observed crystal properties. In practice, it is found that models based on formal charges work well, even for compounds such as silicates and zeolites in which there is a significant degree of covalency.

The simulations of the lithium manganese oxide lattices were performed using two-body potentials for Mn–O, Li–O, and O–O interatomic interactions which have already been successfully applied to model lithium insertion in spinel manganese oxide<sup>19</sup> and with only a small modification of the  $\rho$  parameters for the Mn–O potentials to improve further the structural models of both  $\lambda$ -MnO<sub>2</sub> and LiMn<sub>2</sub>O<sub>4</sub>. The shell model parameters were refined to achieve the best fit of the predicted wavenumbers of infrared and Raman-active vibrations to experimentally observed wavenumbers. These potential and shell model parameters are given in Table 1. The calculated lattice parameters and atomic positions for LiMn<sub>2</sub>O<sub>4</sub> and  $\lambda$ -MnO<sub>2</sub>, after energy minimization to generate a relaxed equilibrium structure, are reported in Table 2. The data show excellent agreement with the experimentally observed structures. To verify the consistency of this model with our previously reported simulations,<sup>19</sup> we calculated a range of interstitial, vacancy, and migration energies. The results agree with the values calculated in our previous model to within  $\pm 2\%$ .

The phonon calculations presented here are based on standard methodology involving the Cartesian second derivative matrix. The vibrational frequencies are the square roots of the eigenvalues of the dynamical matrix, which consists of the mass-weighted second derivatives. Such methods have been used<sup>20–22</sup> to calculate the phonon dispersion curves of oxides, such as

$\alpha$ -SiO<sub>2</sub>, UO<sub>2</sub>, and La<sub>2</sub>CuO<sub>4</sub>, but have rarely been used to interpret the vibrational spectra of solid compounds.

Inserted protons in the spinel manganese oxide were modeled as hydroxyl groups located at oxygen sites in the lattice. The O–H interaction was simulated using an attractive Morse potential

$$V(r) = D\{1 - \exp[-\beta(r - r_0)]\}^2$$

the parameters for which were developed by Saul et al.<sup>23</sup> using ab initio quantum mechanical cluster calculations. The complete set of potential parameters for the hydroxyl group has been described previously.<sup>19</sup> The hydroxyl group in spinel MnO<sub>2</sub> was modeled as an isolated defect species. The method for calculating the vibrational frequencies for such defects involves the calculation of the force constant matrix for the inner defect region. This approach has been effective for localized vibrations, such as an OH group, which are largely decoupled from the lattice phonons.

**2.2. Experimental Section.** A Pt/LiMn<sub>2</sub>O<sub>4</sub> electrode was prepared by a thermal decomposition method as described previously.<sup>24,25</sup> A small amount of a mixed solution of LiNO<sub>3</sub> and Mn(NO<sub>3</sub>)<sub>2</sub> (2 mol/dm<sup>3</sup>, Li/Mn mole ratio = 0.5) was brushed onto a Pt plate (10 × 10 × 0.3 mm<sup>3</sup>) to form a thin layer of the solution. After drying at room temperature, the plate was heated to 1093 K for a few minutes and then cooled to room temperature. This brush–heating treatment was repeated 15 times. Finally, the plate was annealed at 1093 K for 5 min to form the Pt/LiMn<sub>2</sub>O<sub>4</sub> electrode. X-ray diffraction using a Rigaku RINT 1200 diffractometer showed the formation of a uniform spinel phase (space group *Fd3m*) of LiMn<sub>2</sub>O<sub>4</sub> with a lattice parameter of 8.25 Å. The Li/Mn ratio was determined as 0.47 by atomic absorption spectrometry after dissolving the oxide layer with a mixed solution of hydrochloric acid and hydrogen peroxide. The average thickness of the LiMn<sub>2</sub>O<sub>4</sub> layer was calculated as 0.94  $\mu$ m, and the average particle diameter was estimated as 0.50  $\mu$ m by scanning electron microscopy observation.<sup>26</sup>

The electrochemical extraction of lithium from the thin-film coating of LiMn<sub>2</sub>O<sub>4</sub> was carried out by applying a constant potential (1 V vs a saturated calomel electrode) to the Pt/LiMn<sub>2</sub>O<sub>4</sub> electrode in a 0.01 mol/dm<sup>3</sup> LiCl solution at 298 K. After the electric current had decreased from 1.5 mA to less than 5  $\mu$ A, the Pt plate was washed with water and air-dried. The Li/Mn ratio determined by atomic absorption spectrometry was 0.0075, and X-ray diffraction showed that a topotactic Li<sup>+</sup> extraction had occurred with a decrease of the lattice parameter to 8.05 Å, consistent with formation of the phase  $\lambda$ -MnO<sub>2</sub>.

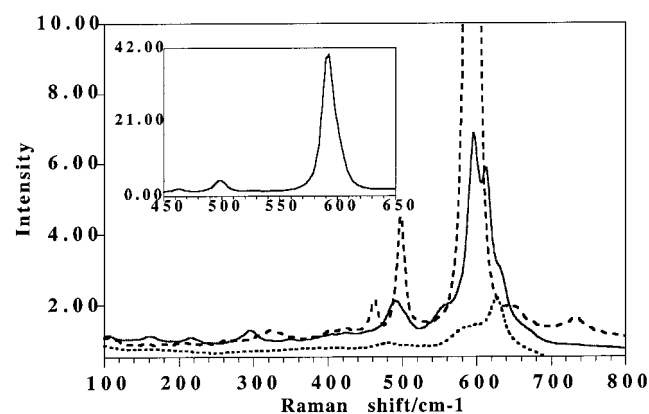
The intermediate spinel phase Li<sub>0.5</sub>Mn<sub>2</sub>O<sub>4</sub> was formed by applying a constant potential of 0.65 V to the Pt/ $\lambda$ -MnO<sub>2</sub> electrode in a 0.01 mol/dm<sup>3</sup> LiCl solution until the current had decreased to less than 5  $\mu$ A.<sup>24</sup> The lattice parameter and the Li/Mn ratio were 8.13 Å and 0.26, respectively, close to those reported elsewhere for Li<sub>0.5</sub>Mn<sub>2</sub>O<sub>4</sub>.<sup>27</sup>

Raman spectra of the thin-film sample were recorded using a Holoprobe 532 Raman system (Kaiser Optical Systems Inc.) with a microscope attachment. Raman data for the bulk-phase samples were recorded in the visible region of the electromagnetic spectrum on a Jobin-Yvon Ramanor U-1000 spectrometer using Spectra-Physics 164 argon-ion and krypton-ion lasers as the excitation source.

Infrared absorption data were measured using a Bomem DA8 Fourier transform spectrometer with the samples prepared as KBr and polyethylene disks.

**TABLE 3: Calculated and Observed Wavenumbers ( $k = 0$ ) for  $\text{LiMn}_2\text{O}_4$  and  $\lambda\text{-MnO}_2$ , Their Corresponding Symmetry Species, and the Predicted Optical Activity**

$\text{LiMn}_2\text{O}_4$		$\lambda\text{-MnO}_2$		symmetry species	activity
calcd	obsd	calcd	obsd		
118		21		$T_{2u}$	inactive
287	277			$T_{1u}(1)$	IR
317		310		$E_u$	inactive
354	365			$T_{2g}(1)$	Raman
357		316		$T_{1g}$	inactive
383	360	371		$T_{1u}(2)$	IR
434	432	479	463	$E_g$	Raman
454		436		$T_{2u}$	inactive
455	480	511	498	$T_{2g}(2)$	Raman
517	513	549	543	$T_{1u}(3)$	IR
570		540		$A_{2u}$	inactive
570		599		$E_u$	inactive
597	590	630	647	$T_{2g}(3)$	Raman
598	625	592	592	$A_{1g}$	Raman
633	615	618	610	$T_{1u}(4)$	IR
649		629		$A_{2u}$	inactive

**Figure 1.** Raman spectra for  $\text{Li}_x\text{Mn}_2\text{O}_4$  ( $x = 0.969$  (---);  $x = 0.494$  (—);  $x = 0.015$  (- - -)). Inset shows the full spectrum for the resonance-enhanced,  $x = 0.015$  sample, from 450 to 650  $\text{cm}^{-1}$ .

### 3. Results and Discussion

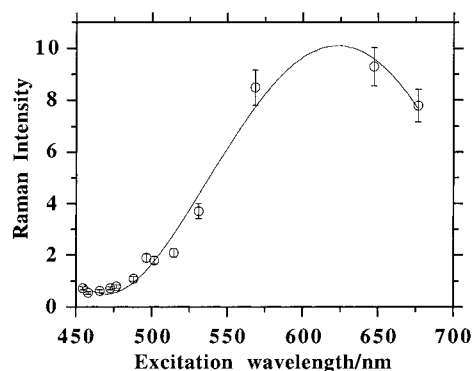
The wavenumbers, symmetry species, and optical activities of the lattice vibrations calculated for  $\text{LiMn}_2\text{O}_4$  and  $\lambda\text{-MnO}_2$  are given in Table 3. The assumption made for both lattices is that cations and oxygen anions are completely ordered, whereas the reality is that these spinel lattices have varying degrees of disorder due to the loss of translational invariance associated with the presence of the Jahn-Teller unstable  $\text{Mn}^{3+}$  cation in  $\text{LiMn}_2\text{O}_4$  and with the nonstoichiometry of the partially delithiated phases.

The number of lattice phonons and their symmetry species agree with factor group analyses for the primitive rhombohedral Bravais cells.<sup>28</sup> For  $\text{LiMn}_2\text{O}_4$ , there are 39 phonons distributed as

$$\Gamma = A_{1g} + E_g + T_{1g} + 3T_{2g} + A_{2u} + 2E_u + 4T_{1u} + 2T_{2u}$$

and there are 33 for  $\lambda\text{-MnO}_2$ , where removal of the lithium atom results in the loss of  $T_{2g}$  and  $T_{1u}$  phonons.

**3.1. Raman Spectra of  $\text{Li}_x\text{Mn}_2\text{O}_4$ .** Experimental Raman spectra of thin-film  $\text{LiMn}_2\text{O}_4$ , measured using 532 nm excitation, are shown at various stages of electrochemical delithiation in Figure 1. The spectrum of  $\text{LiMn}_2\text{O}_4$  presents a number of broad bands, while the maximally delithiated sample shows a series of bands of much greater intensity. As shown in Figure 2, resonance enhancement of the Raman spectrum occurs for the delithiated spinel,  $\lambda\text{-MnO}_2$ , with a  $\lambda_{\text{max}}$  for the excitation profile

**Figure 2.** Resonance Raman excitation profile for the  $A_{1g}$  phonon in polycrystalline  $\lambda\text{-MnO}_2$ .

of ca. 620 nm. No significant resonance enhancement has been observed for  $\text{LiMn}_2\text{O}_4$  measured over the same wavelength range. The presence of resonance enhancement of the  $\lambda\text{-MnO}_2$  phonons may be explained in terms of B term scattering involving vibronic states of  $\text{Mn}^{4+}$ .<sup>29</sup> Further studies of the ultraviolet and visible absorption spectra of lithium manganate spinels are being undertaken, and these will provide insight into the precise mechanism for the observed enhancement.

In the absence of single-crystal data, it is difficult to assign bands in the Raman spectra to modes of different symmetry. Interpretation is further complicated by the appearance of a higher number of vibrations in the experimental spectra than are predicted by group theory for the perfectly cubic compound. There is therefore a need for a theoretical model to understand the data.

Calculations predict five Raman-active modes for  $\text{LiMn}_2\text{O}_4$ , one of  $A_{1g}$  symmetry, one of  $E_g$  symmetry, and three of  $T_{2g}$  symmetry. The calculated atomic displacements for each of these phonons are illustrated in Figure 3. The Mn ions are motionless for all of the eigenvectors. The  $A_{1g}$  and  $E_g$  vibrations involve only oxide ion displacements. The  $T_{2g}(2)$  and  $T_{2g}(3)$  phonons are characterized by large oxygen motions and very small Li displacements, but the lowest energy  $T_{2g}(1)$  phonon derives predominantly from a vibration of the Li sublattice. It is this latter mode that is predicted to disappear when the lattice is completely delithiated.

The experimental Raman data for  $\text{LiMn}_2\text{O}_4$  consist of a series of broad bands between 300 and 700  $\text{cm}^{-1}$ . The  $T_{2g}(1)$  mode which we calculate at 354  $\text{cm}^{-1}$  and the  $E_g$  mode at 434  $\text{cm}^{-1}$  are visible as weak features at ca. 365 and 432  $\text{cm}^{-1}$  in the data for bulk-phase  $\text{LiMn}_2\text{O}_4$  but are not resolved in the data for the thin film. However, both sets of data show bands at ca. 480, 590, and 625  $\text{cm}^{-1}$ . Our calculations assign the band at 480  $\text{cm}^{-1}$  to the  $T_{2g}(2)$  phonon. The calculated values for the  $T_{2g}(3)$  and  $A_{1g}$  phonons in  $\text{LiMn}_2\text{O}_4$  are very close (597 and 598  $\text{cm}^{-1}$ , respectively) and prevent unambiguous assignment of the two higher energy Raman bands. However, the highest energy band at 625  $\text{cm}^{-1}$  has a narrower line width in the experimental data compared to the other Raman bands, suggesting that it derives from the totally symmetric  $A_{1g}$  vibration. It is likely that the calculation slightly underestimates (by ca. 4%) the wavenumber of the  $A_{1g}$  mode in the case of  $\text{LiMn}_2\text{O}_4$ , as this mode is mainly sensitive to the oxygen shell parameters which were transferred without change from the  $\lambda\text{-MnO}_2$  model.

When the lattice is fully electrochemically delithiated to a composition  $\text{Li}_{0.015}\text{Mn}_2\text{O}_4$ , termed  $\lambda\text{-MnO}_2$ , the  $T_{2g}(2)$  and  $T_{2g}(3)$  phonons become modes of oxygen ions only and, along with the  $E_g$  mode, are predicted to increase in wavenumber. The wavenumber of the  $A_{1g}$  mode is predicted to decrease. The



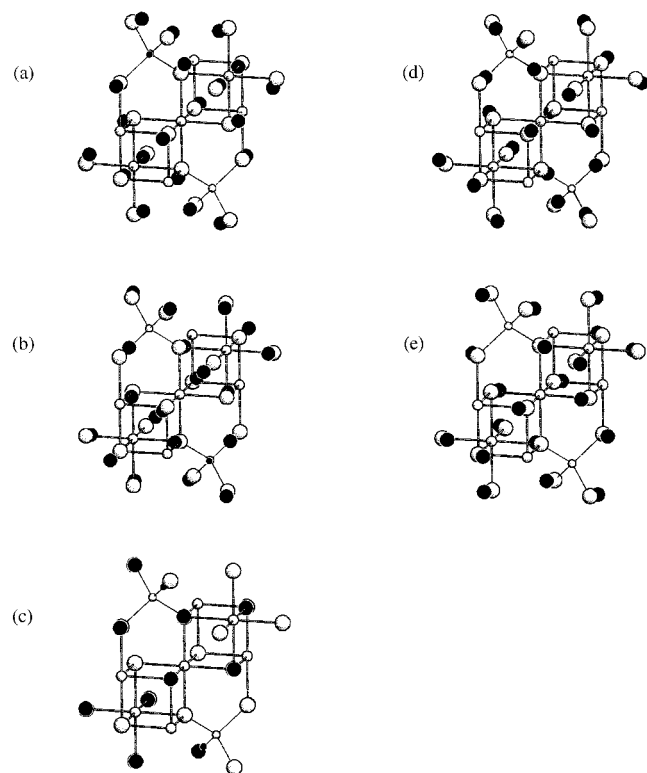


**Figure 3.** Cartesian displacements for the  $T_{2g}(3)$  (a),  $T_{2g}(2)$  (b),  $T_{2g}(1)$  (c),  $A_{1g}$  (d), and  $E_g$  (e) modes of  $\text{LiMn}_2\text{O}_4$ . The atomic positions for the equilibrium structure are shown as open spheres and for the displaced atoms as filled spheres.

experimental data for  $\lambda\text{-MnO}_2$  supports these predictions. In the resonance enhanced spectrum, three strong bands appear at 463, 498, and 592  $\text{cm}^{-1}$  and there is a shoulder at 647  $\text{cm}^{-1}$ . This latter band correlates with a similar band observed at 647  $\text{cm}^{-1}$  in the Raman spectra of the  $\text{Mn}^{4+}$  oxides pyrolusite and ramsdellite.<sup>30</sup> The calculations assign the bands, in order of increasing wavenumber, to the  $E_g$ ,  $T_{2g}(2)$ ,  $A_{1g}$ , and  $T_{2g}(3)$  phonons. The strong intensity enhancement of the band at 592  $\text{cm}^{-1}$  is consistent with its assignment as the  $A_{1g}$  mode.

For compositions intermediate between  $\text{LiMn}_2\text{O}_4$  and  $\lambda\text{-MnO}_2$ , the symmetry, and in particular the local symmetry, will no longer belong to the  $Fd3m$  space group. Certain modes which are Raman inactive under  $Fd3m$  will therefore appear in the Raman spectrum for these partially delithiated compounds. To investigate this aspect, we modeled the  $\text{Li}_{0.5}\text{Mn}_2\text{O}_4$  spinel phase in the  $F43m$  space group, which is a lower symmetry subgroup of  $Fd3m$ . In this structure, every second lithium tetrahedral site is vacant, producing an ordered Li configuration which has been experimentally observed for this composition.<sup>26,31</sup>

The calculation for  $\text{Li}_{0.5}\text{Mn}_2\text{O}_4$  (Table 4) shows six phonons of  $T_2$  symmetry, three of  $T_1$  symmetry, three of  $E$  symmetry, and three of  $A_1$  symmetry. The  $A_1$  modes,  $E$  modes, and six  $T_2$  modes are predicted to be Raman active. Of the three  $A_1$  modes, one is related to the Raman-active  $A_{1g}$  mode in  $\text{LiMn}_2\text{O}_4$  and  $\lambda\text{-MnO}_2$  and the other two derive from the previously optically inactive  $A_{2u}$  phonons. Similarly, of the three  $E$  modes, one is related to the Raman-active  $E_g$  mode in  $\text{LiMn}_2\text{O}_4$  and  $\lambda\text{-MnO}_2$  and the other two derive from the previously optically inactive  $E_u$  phonons. Three of the  $T_2$  modes derive from the Raman-active  $T_{2g}$  modes in  $\text{LiMn}_2\text{O}_4$  and  $\lambda\text{-MnO}_2$ , while the other three correspond to infrared-active  $T_{1u}$  modes which become Raman-active under  $F43m$ .

As predicted by the calculations, the experimental spectrum for  $\text{Li}_{0.5}\text{Mn}_2\text{O}_4$  (Figure 1) shows a richer structure than either

**TABLE 4: Calculated and Observed Wavenumbers ( $k = 0$ ) for  $\text{Li}_{0.5}\text{Mn}_2\text{O}_4$ , Assuming a  $F43m$  Space Group, Their Corresponding Symmetry Species, and the Predicted Optical Activity**

$\text{Li}_{0.5}\text{Mn}_2\text{O}_4$		symmetry species	activity
calcd	obsd		
80		$T_1$	inactive
313	296	$T_2$	IR and Raman
317		$E$	Raman
342		$T_1$	inactive
385		$T_2$	IR and Raman
449		$T_1$	inactive
457		$E$	Raman
481	493	$T_2$	IR and Raman
537		$T_2$	IR and Raman
559	560	$A_1$	Raman
586		$E$	Raman
593	597	$A_1$	Raman
615	612	$T_2$	IR and Raman
646	630	$T_2$	IR and Raman
665	657	$A_1$	Raman

$\text{LiMn}_2\text{O}_4$  or  $\lambda\text{-MnO}_2$ , particularly in the envelope of overlapping bands between 520 and 680  $\text{cm}^{-1}$ . The two most intense bands at 597 and 612  $\text{cm}^{-1}$  are assigned to the modes of  $A_1$  and  $T_2$  symmetry derived from the Raman-active  $A_{1g}$  and  $T_{2g}(3)$  modes under  $Fd3m$ . The shoulders on either side of these two bands can derive from the Raman activation of the infrared active  $T_{1u}(3)$  and  $T_{1u}(4)$  modes under  $Fd3m$  and from the previously optically inactive modes of  $A$  symmetry with calculated wavenumbers ca. 559 and 665  $\text{cm}^{-1}$ . In the lower wavenumber part of the spectrum, bands at ca. 160, 216, and 296  $\text{cm}^{-1}$  in the experimental data appear to be associated particularly with the  $\text{Li}_{0.5}\text{Mn}_2\text{O}_4$  phase. The band at 296  $\text{cm}^{-1}$  can be assigned to activation of either the infrared active  $T_{1u}(1)$  mode of predominantly Li vibrational character or the  $E$  mode in this region of the spectrum. Our calculations using  $Fd3m$  or its subgroups calculate only the inactive  $T_{2u}$  mode as having a wavenumber below 250  $\text{cm}^{-1}$ . A possible explanation for these low-wavenumber bands is that they are attributable to the two-phase system claimed by Xia et al.<sup>32</sup> for electrochemically delithiated  $\text{LiMn}_2\text{O}_4$ . However, while there are low-wavenumber bands in the Raman spectra of the proposed second-phase compounds  $\text{Mn}_2\text{O}_3$  and  $\text{Mn}_3\text{O}_4$ , both have bands at 690 and 659  $\text{cm}^{-1}$ , respectively,<sup>30</sup> which are absent from the spectra shown in Figure 1. The two low-wavenumber Raman bands observed for  $\text{Li}_{0.5}\text{Mn}_2\text{O}_4$  cannot therefore be explained in terms of either of these oxides as a second phase but may be attributable to a supercell configuration or to gap modes of defect sites, structural features that are outside the scope of the model used here.

**3.2. Infrared Spectra.** The calculations predict that four vibrational modes will appear in the infrared spectrum for  $\text{LiMn}_2\text{O}_4$  and three for  $\lambda\text{-MnO}_2$ . The infrared spectra of spinel lithium manganese oxides typically show broad bands, which has led to disagreement as to the assignment of the fundamental vibrations. Our calculations for  $\text{LiMn}_2\text{O}_4$  predict two higher wavenumber modes, at 517 and 633  $\text{cm}^{-1}$ , and two lower wavenumber modes at 287 and 383  $\text{cm}^{-1}$ . Experimentally, the former modes are observed<sup>1,8,9</sup> as intense broad bands, easily resolved in the mid-infrared region. The band that we calculate at 383  $\text{cm}^{-1}$  appears as a shoulder at ca. 360  $\text{cm}^{-1}$  on the broad band at 513  $\text{cm}^{-1}$ . The calculated band at 287  $\text{cm}^{-1}$  has been reported as a relatively weak absorption at 277  $\text{cm}^{-1}$  and assigned as a deformation vibration of the  $\text{MnO}_6$  octahedron.<sup>9</sup>

The calculations predict only small changes in the wavenumbers of the three higher energy infrared bands when

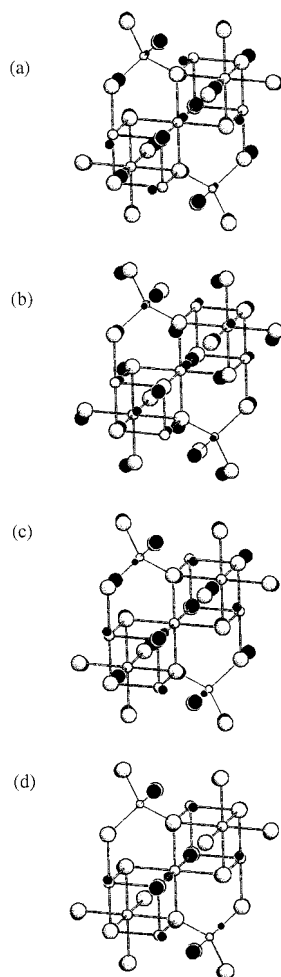


**Figure 4.** Cartesian displacements for the  $T_{1u}(4)$  (a),  $T_{1u}(3)$  (b),  $T_{1u}(2)$  (c), and  $T_{1u}(1)$  (d) modes of  $\text{LiMn}_2\text{O}_4$ . The atomic positions for the equilibrium structure are shown as open spheres and for the displaced atoms as filled spheres.

$\text{LiMn}_2\text{O}_4$  is delithiated to give  $\lambda\text{-MnO}_2$ , in agreement with experimental observations. The  $287\text{ cm}^{-1}$  mode is predicted to disappear on delithiation. To better understand these changes, the calculated atomic displacements for the infrared-active phonons in  $\text{LiMn}_2\text{O}_4$  are shown in Figure 4. It is now accepted<sup>33</sup> that the atomic displacements contributing to the infrared spectra of spinel phases are complex vibrations of the entire lattice and therefore vary considerably from compound to compound, depending on the masses, charges, and chemical properties of the ions. This is because the infrared-active modes all belong to the same symmetry species,  $T_{1u}$ , and can interact strongly with one another. It can be seen in Figure 4 that the two higher wavenumber modes involve mainly displacements of oxide ions, although the vibrations are rather more complex than the simple Mn–O stretching to which these bands are often loosely assigned. The modes at  $383$  and  $287\text{ cm}^{-1}$  also involve displacements of all the ions in the lattice but derive predominantly from cooperative vibrations of Mn and Li ions, respectively. The mode that has its principal origins in vibrations of the Li sublattice is the one which disappears on removal of lithium from the lattice. Other than the removal of the Li contributions, the eigenvectors for the other three infrared-active phonons change very little between  $\text{LiMn}_2\text{O}_4$  and  $\lambda\text{-MnO}_2$ . We note that our calculated eigenvectors for the infrared modes agree qualitatively with experimental analyses of the dominant contributions to each of the four infrared bands for normal II, III spinels.<sup>34</sup> These empirical comparisons for a range of spinel

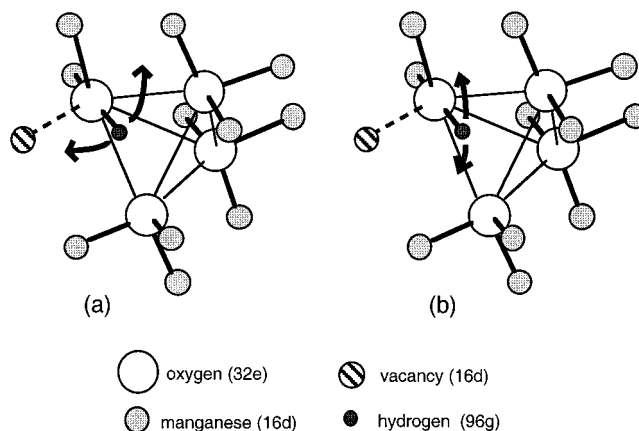


**Figure 5.** Displacements of the hydroxyl proton in the orthogonal deformation vibrations calculated for the hydroxyl species coordinating a 16d Mn vacancy: (a)  $871\text{ cm}^{-1}$ ; (b)  $925\text{ cm}^{-1}$ .

compounds show the dominant contributions of oxygen to the two higher energy bands, of the octahedral cation to the bands typically observed in the range  $300\text{--}450\text{ cm}^{-1}$ , and of the tetrahedral cation to the bands in the  $100\text{--}300\text{ cm}^{-1}$  range.

**3.3. Protons in  $\lambda\text{-MnO}_2$ .** The interatomic potential model can be extended to perform a vibrational analysis for lattice protons in  $\lambda\text{-MnO}_2$ . Protons are inserted into spinel lithium manganese oxides in acidic solutions by exchange with Li ions when the compound contains vacancies on 16d octahedral sites.<sup>2,35,36</sup> Neutron diffraction and inelastic neutron scattering spectroscopy have identified the lattice protons in spinel  $\text{MnO}_2$  as hydroxyl species orientated toward neighboring oxygen ions across the interstitial channels vacated by the Li ions.<sup>37</sup> This places the hydroxyl protons in 96g sites in space group  $Fd3m$ , although only a fraction of the sites are actually occupied in the compound. Atomistic modeling methods have previously predicted that the hydroxyl proton will relax to this position when the nearest 16d octahedral site is vacant.<sup>19</sup>

Hydroxyl in spinel  $\text{MnO}_2$  was modeled as an isolated defect species substituting an oxide ion in the spinel  $\text{MnO}_2$  lattice. A vacancy was introduced at one of the three Mn sites coordinated by the hydroxyl oxygen, as described in ref 19. This model places the hydroxyl proton in the 96g site determined by the neutron diffraction study.<sup>37</sup> Vibrational frequencies were then calculated for the two orthogonal deformation modes of this hydroxyl group illustrated in Figure 5.

The wavenumbers for the deformation modes calculated using this model are  $871$  and  $925\text{ cm}^{-1}$ . In the infrared spectrum, protonated forms of spinel  $\text{MnO}_2$  are characterized by a band with a maximum at  $908\text{ cm}^{-1}$  and a shoulder at  $870\text{ cm}^{-1}$ , shown in Figure 6. The  $908\text{ cm}^{-1}$  vibration produces the most intense band in inelastic neutron scattering spectroscopy, confirming that it derives from a hydroxyl deformation mode.<sup>35</sup> This band has a shoulder<sup>36</sup> at  $870\text{ cm}^{-1}$  that corresponds to the feature observed in the infrared absorption spectrum. The good agreement between the calculated and observed wavenumbers supports the assignment of the two observed bands to orthogonal vibrations of the same hydroxyl group.

To compare with the above model, vibrational modes were also calculated for a hydroxyl orientation in which the proton is directed toward the center of the vacant 8a tetrahedron. This more symmetric orientation is calculated to be the fully relaxed configuration if all three Mn sites coordinated by the hydroxyl oxygen are occupied.<sup>19</sup> For this configuration, the two orthogonal bending modes of the hydroxyl are calculated to be degenerate with a wavenumber of  $1030\text{ cm}^{-1}$ . Although the

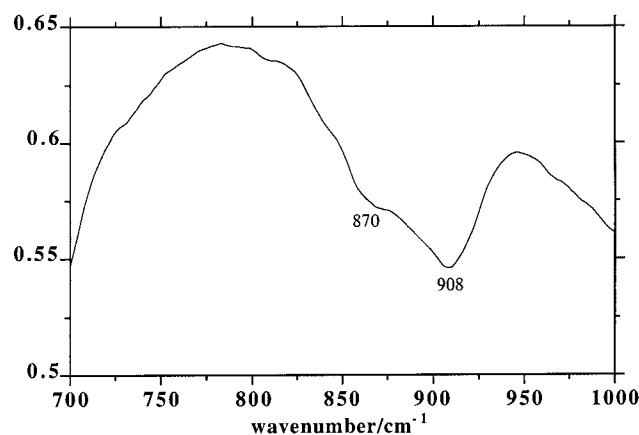


**Figure 6.** Infrared absorption spectrum for  $\lambda$ -MnO<sub>2</sub> showing the two deformation modes assigned to the inserted proton in the 96g sites of the spinel lattice.

infrared spectrum of protonated spinel MnO<sub>2</sub> shows some broad absorption between 1000 and 1100 cm<sup>-1</sup>, inelastic neutron scattering has shown that these bands do not correspond to vibrations involving hydrogen. It can be concluded, in agreement with previous results, that protons do not occupy this type of symmetric site in spinel MnO<sub>2</sub>.

#### 4. Conclusions

The eigenvectors calculated using the simulation methods described here allow the fundamental vibrations appearing in the infrared and Raman spectra of spinel lithium manganese oxides to be identified and described. The model can furthermore be extended to interpret the vibrations of protons inserted into the oxide lattice by lithium–proton exchange. These results confirm our previous model for the hydroxyl group in which the hydroxyl protons occupy the 96g sites of the *Fd3m* space group, with one of the three Mn sites coordinated by the hydroxyl oxygen remaining vacant.

The complex changes observed for the Raman spectra of lithium manganate spinels on delithiation have been largely explained in terms of the appearance of additional Raman-active modes of the lower symmetry Li<sub>0.5</sub>Mn<sub>2</sub>O<sub>4</sub> phase. These new data are further confirmation of the fact that the Li ions are ordered in this partially delithiated phase.

These lattice simulation methods have rarely been used to interpret the vibrational spectra of oxide compounds, and yet the approach offers considerable flexibility. In particular, the energy minimization procedures allow fully relaxed local structures around lattice defects to be calculated and the resulting perturbations to the vibrational spectra to be predicted. This approach should aid in identifying the structural origins of the variations in the vibrational spectra of lithium manganates which occur as a result of different preparation conditions or in the course of lithium extraction–insertion cycles.

**Acknowledgment.** We thank the Royal Society (London) for support through the European Science Exchange Program, the New Zealand Foundation for Research, Science, and Technology for a Science and Technology Postdoctoral Fel-

lowship (B.A.), and la Ministère de L'Éducation Nationale de L'Enseignement Supérieur et de la Recherche pour la Bourse de Haut Niveau', MENESR (G.R.B.). The simulations were carried out on the supercomputers at the Rutherford Appleton Laboratory, UK.

#### References and Notes

- (1) Richardson, T. J.; Wen, S. J.; Striebel, K. A.; Ross, P. N., Jr.; Cairns, E. J. *Mater. Res. Bull.* **1997**, *32*, 609.
- (2) Feng, Q.; Miyai, H.; Kanoh, H.; Ooi, K. *Langmuir* **1992**, *8*, 1861.
- (3) Preudhomme, J.; Tarte, P. *Spectrochim. Acta* **1971**, *27A*, 845.
- (4) Preudhomme, J.; Tarte, P. *Spectrochim. Acta* **1973**, *29A*, 1301.
- (5) Schutte, L.; Coismann, G.; Reuter, B. *J. Solid State Chem.* **1979**, *27*, 227.
- (6) Liu, Y.; Feng, Q.; Ooi, K. *J. Colloid Interface Sci.* **1994**, *163*, 130.
- (7) Feng, Q.; Kanoh, H.; Miyai, H.; Ooi, K. *Chem. Mater.* **1975**, *7*, 379.
- (8) Wolska, E.; Stempin, K.; Krasnowska-Hobbs, O. *Solid State Ionics* **1997**, *101–103*, 527.
- (9) Julien, C.; Massot, M.; Pirez-Vicente, C.; Haro-Poniatowski, E.; Nazri, G. A.; Rougier, A. *Mater. Res. Soc. Symp. Proc.* **1998**, *496*, 415.
- (10) (a) Catlow, C. R. A. In *Solid State Chemistry Techniques*; Cheetham, A. K., Day, P., Eds.; Clarendon Press: Oxford, 1987; Chapter 7. (b) Catlow, C. R. A.; Price, G. D. *Nature* **1990**, *347*, 243.
- (11) Dick, B. G.; Overhauser, A. W. *Phys. Rev.* **1958**, *112*, 90.
- (12) Mott, N. F.; Littleton, M. J. *Trans. Faraday Soc.* **1938**, *34*, 485.
- (13) (a) Gale, J. D. *GULP* (General Utility Lattice Program); Royal Institution of GB and Imperial College: London, 1991–1996. (b) Gale, J. D. *J. Chem. Soc., Faraday Trans.* **1997**, *93*, 629.
- (14) Cherry, M.; Islam, M. S.; Catlow, C. R. A. *J. Solid State Chem.* **1995**, *118*, 125.
- (15) Cherry, M.; Islam, M. S.; Gale, J. D.; Catlow, C. R. A. *J. Phys. Chem.* **1995**, *99*, 14614.
- (16) Islam, M. S.; Cherry, M.; Winch, L. J. *J. Chem. Soc., Faraday Trans.* **1996**, *92*, 479.
- (17) Wu, J. W.; Tepesch, P. D.; Ceder, G. *Philos. Mag. B* **1998**, *77*, 1039.
- (18) Balducci, G.; Kaspar, J.; Fornasiero, P.; Graziani, M.; Islam, M. S.; Gale, J. D. *J. Phys. Chem. B* **1997**, *101*, 1750.
- (19) Ammundsen, B.; Rozière, J.; Islam, M. S. *J. Phys. Chem. B* **1997**, *101*, 8156.
- (20) Schröder, K.-P.; Sauer, J. *J. Phys. Chem.* **1996**, *100*, 11043.
- (21) Jackson, R. A.; Murray, A. D.; Harding, J. H.; Catlow, C. R. A. *Philos. Mag. A* **1986**, *53*, 27.
- (22) Islam, M. S.; Leslie, M.; Tomlinson, S. M.; Catlow, C. R. A. *J. Phys. C: Solid State Phys.* **1988**, *21*, L109.
- (23) Saul, P.; Catlow, C. R. A.; Kendrick, J. *Philos. Mag. B* **1985**, *51*, 107.
- (24) Kanoh, H.; Ooi, K.; Miyai, Y.; Katoh, S. *Langmuir* **1991**, *7*, 1841.
- (25) Kanoh, H.; Ooi, K.; Miyai, Y.; Katoh, S. *Sep. Sci. Technol.* **1993**, *28*, 643.
- (26) Kanoh, H.; Feng, Q.; Miyai, Y.; Ooi, K. *J. Electrochem. Soc.* **1995**, *142*, 702.
- (27) Ooi, K.; Miyai, Y.; Katoh, S.; Maeda, H.; Abe, M. *Langmuir* **1989**, *5*, 150.
- (28) White, W. B.; De Angelis, B. A. *Spectrochim. Acta* **1967**, *23A*, 985.
- (29) Clark, R. J. H.; Dines, T. J. In *Advances In Infrared and Raman Spectroscopy*; Clark, R. J. H., Hester, R. E., Eds.; Heyden: London, 1975; Vol. 9, Chapter 5.
- (30) Burns, G. R. Unpublished data.
- (31) Gao, Y.; Reimers, J. N.; Dahn, J. R. *Phys. Rev. B* **1996**, *54*, 3878.
- (32) Xia, Y.; Zhou, Y.; Yoshio, M. *J. Electrochem. Soc.* **1997**, *144*, 2593.
- (33) Himmrich, J.; Lutz, H. D. *Solid State Commun.* **1991**, *79*, 447.
- (34) Preudhomme, J.; Tarte, P. *Spectrochim. Acta* **1971**, *27A*, 1817.
- (35) Ammundsen, B.; Burns, G. R.; Jones, D. J.; Rozière, J. *Chem. Mater.* **1995**, *7*, 2151.
- (36) Ammundsen, B.; Aitchison, P. B.; Burns, G. R.; Jones, D. J.; Rozière, J. *Solid State Ionics* **1997**, *97*, 269.
- (37) Ammundsen, B.; Jones, D. J.; Rozière, J.; Berg, H.; Tellgren, R.; Thomas, J. O. *Chem. Mater.* **1998**, *10*, 1680.